UC Berkeley
UC Berkeley Previously Published Works

Title

Unraveling the Highly Plastic Behavior of ALD-Aluminum Oxide Encapsulations by Small-Scale Tensile Testing

Permalink

https://escholarship.org/uc/item/90n1z03k

Journal

Advanced Engineering Materials, 26(8)

ISSN

1438-1656

Authors

Vogl, Lilian M

Schweizer, Peter

Minor, Andrew M

et al.

Publication Date

2024-04-01

DOI

10.1002/adem.202302220

Copyright Information

Peer reviewed

Unraveling the Highly Plastic Behavior of ALD-Aluminum Oxide Encapsulations by Small-Scale Tensile Testing

Lilian M. Vogl,* Peter Schweizer, Andrew M. Minor, Johann Michler, and Ivo Utke

We present a study directly measuring the electron-beam-induced plasticity of amorphous Al_2O_3 coatings. Core–shell nanostructures are employed as small-scale model systems for two-dimensional coatings made by atomic layer deposition (ALD). Copper nanowires (NWs) are used as substrates for ALD deposition, representing a model system for interconnects commonly found in integrated circuits. Experiments are performed in situ in a transmission electron microscope (TEM) and further analyzed with electron energy loss spectroscopy (EELS). Our in situ TEM tensile experiments reveal the highly plastic behavior of the ALD shell, which withstands a maximum strain of 188%. Comparable samples under beam-off conditions show a brittle fracture, which underlines the effect of electron irradiation. The electron-beam-activated bond switching within the amorphous network enables compensation of the applied tensile strain, leading to viscous flow. By incorporating an intermediate nanocrystalline layer within the Al_2O_3 shell, the plasticity is suppressed and brittle fracture occurs. This work directly demonstrates the tuning of mechanical properties in amorphous ALD structures through electron irradiation.

1. Introduction

The deposition of thin films is a common strategy to protect a material against degradation[1,2] and to further enhance the mechanical stability.[3] Depending on the surface characteristic to be improved and the application, such coatings can be made of ceramics,[4] metals/alloys,[5] or metal oxides.[6] In the past,

great progress has been made to improve the reliability of micro-electromechanical systems (MEMS) by depositing a thin metal oxide film via atomic layer deposition (ALD).[7–10] Aluminum oxide represents a standard material for ALD deposition, and the process based on the precursor gases, water, and trimethylaluminium has been studied extensively.[11] Without post annealing at high temperatures $\geq 900\,°C,$[12,13] the as-deposited ALD-Al_2O_3 films are amorphous. The insulating nature[14] and the precise nanometer-level thickness control of ALD-Al_2O_3 make it an ideal choice as a dielectric material and protective coating, particularly on small scales. To further push the development of efficient coatings, it is crucial to characterize the coating material in more detail. Several studies have analyzed the mechanical properties of metal oxide films.[15–18] However, the sample preparation is time-consuming, and underlying substrates[19] can crucially affect the measurement. In addition, conventional strategies to strengthen the material, like work hardening[20] or grain boundary strengthening,[21] cannot be applied for standard ALD-Al_2O_3, as amorphous structures have no long-range periodicity. Therefore, alternative methods to tailor the mechanical properties of amorphous ALD coatings are required. For silica glass, high-energy irradiation[22–24] has been reported to activate an atomic-scale rearrangement mechanism. The influence of electron irradiation on the deformation behavior of nanoscale silica glass has already been analyzed by in situ transmission electron microscopy (TEM).[25,26]

In this study, we will demonstrate and analyze the electron-beam-induced plasticity of amorphous ALD-Al_2O_3 coatings. Core–shell nanostructures are used as equivalent small-scale model systems for two-dimensional coatings. The electron microscopy study includes in situ tensile testing inside the TEM as well as the analysis of samples strained under beam-off conditions, demonstrating the need of the electron beam to enable the brittle-to-ductile transition. The induced plasticity of the amorphous ALD-Al_2O_3 can be suppressed by bringing in intermediate layers of nanocrystalline ALD-ZnO, which shifts the failure toward brittle cracking along grain boundaries. Complementary electron energy loss spectroscopy (EELS) is utilized to analyze changes occurring within the amorphous network as a result of electron beam exposure.

L. M. Vogl, P. Schweizer, J. Michler, I. Utke
Laboratory for Mechanics of Materials & Nanostructures
Swiss Federal Laboratories for Materials Science and Technology (Empa)
Thun 3603, Switzerland
E-mail: Lilian.Vogl@berkeley.edu

L. M. Vogl, A. M. Minor
Department of Materials Science and Engineering
University of California
Berkeley, CA 94720, USA

P. Schweizer, A. M. Minor
Lawrence Berkeley National Laboratory
Molecular Foundry
National Center for Electron Microscopy (NCEM)
Berkeley, CA 94720, USA

The ORCID identification number(s) for the author(s) of this article can be found under https://doi.org/10.1002/adem.202302220.

2. Small-Scale Model System for ALD Coatings

For our TEM study, we created core–shell nanostructures that represent small-scale model systems for ALD encapsulations. Copper nanowires (NWs) act as core materials that are produced by an established routine using a sputtering procedure at elevated temperatures.[27] Such metallic NWs are known for their high aspect ratio and their high quality.[28,29]

The NWs emerge from a substrate piece and are subsequently coated via ALD. We use the established process for ALD-Al$_2$O$_3$ coatings[30] based on the two precursors water and TMA. For ZnO deposition, we use water in combination with the precursor diethyl zinc.[31] **Figure 1** gives an overview of the tested sample systems. The core–shell samples (Figure 1a–c) are Cu NWs with thicknesses between 20 and 100 nm, which are conformally coated with Al$_2$O$_3$. The ALD-Al$_2$O$_3$ layer is amorphous for all different layer thicknesses and has a dense and compact appearance without the presence of pores or inclusions. For the ex situ study under the beam-off condition, we varied the shell thickness between 5 and 150 nm. The in situ straining was performed with a 67.9 ± 2.4 nm Al$_2$O$_3$ layer. Figure 1b shows the energy-dispersive X-ray spectroscopy (EDX) mapping of a representative core–shell sample in TEM, and Figure 1c shows the corresponding line scan illustrating the core–shell structure. The nanolaminate samples (Figure 1d,e) consist of alternating ALD layers of Al$_2$O$_3$ and ZnO on Cu NWs. The total shell thickness is 83.2 ± 1.4 nm with five layers of Al$_2$O$_3$ (12.1 ± 0.7 nm) and four layers of ZnO (6.9 ± 0.6 nm), starting and ending with Al$_2$O$_3$. The lower thickness of the ZnO layer results from the etching of the Zn by TMA during the Al$_2$O$_3$ cycle, which reduces the initial growth rate of the ALD-ZnO.[32] Figure 1d shows an EDX mapping of a representative nanolaminate sample with the Al, Zn, and Cu signals. The corresponding line scan across the sample is shown in Figure 1e. We used the same sample batch for in situ and ex situ testing.

3. Results

3.1. Tensile Testing

With an in situ straining holder for the TEM, we applied a mechanical stimulus to observe the response of the material directly (see also description in Section 6 and Figure S1 and S2, Supporting Information). **Figure 2**a shows a core–shell NW for in situ testing before applying tensile strain. An intermediate overview image of the strained sample is shown in Figure 2b. Figure 2e shows the fractured sample after testing. During straining, we observed localized necking at the metallic core (at 2.8% strain) while the ALD shell was still intact, see corresponding image sequence in Figure 2d. The copper NW deforms plastically, which leads to ductile fracture at 8.2% strain. The surrounding shell did not visibly deform, and we do not observe cracking although the core is already completely fractured, see Figure 2c. After the failure of the core, we proceeded with loading to observe the fracture of the shell. Figure 2g shows a close-up image sequence of the in situ testing, demonstrating the rubber-like extension of the ALD shell. The two broken ends of the NW are more and more separated during straining, and a second localized necking spot is introduced (highlighted with the white arrow in Figure 2g). The shell, however, resists the mechanical load and deforms under plastic flow. Figure 2f shows one end of the completely failed core–shell structure after 188% strain.

We focused on elucidating the potential effect of the electron beam on the deformation by performing additional ex situ experiments. **Figure 3** represents a comprehensive overview of the results from these tests. We compared the tensile behavior under beam-on and beam-off conditions. The difference in mechanical deformation is significant for the core–shell samples. Without the electron irradiation, the Al$_2$O$_3$ shell behaves as expected with a brittle fracture, exemplarily displayed in Figure 3a. Such a brittle fracture is generally characterized by a rapid material failure in which no apparent plastic deformation has occurred prior to that. The cracking is initialized starting from the coating and propagates straight until the crack reaches the metallic core. The in situ test indicates a different fracture behavior compared to the ex situ core–shell samples (see Figure 3b). The reason for the changing mechanical deformation from brittle cracking to a viscoplastic flow of the shell can be explained by the electron beam illumination during testing, which will be discussed later.

We analyzed the nanolaminate samples to see the effect of intermediated crystalline ALD layers and the resulting laminated structure on the mechanical behavior. Figure 3 shows the results of the in situ straining test inside the TEM of a nanolaminate sample (Figure 3d) and an exemplary image of a sample that
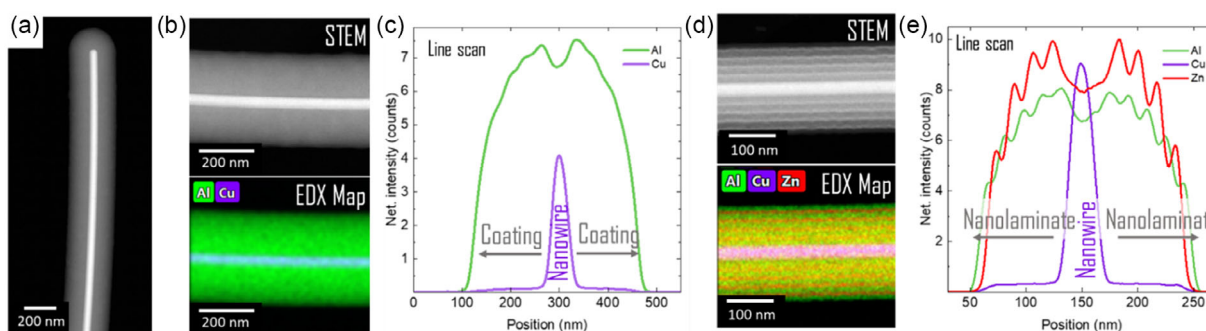
Figure 1. Overview of the sample systems. a) Example STEM image of a core–shell sample: Cu NW coated with a layer of Al$_2$O$_3$. b) STEM image and corresponding EDX mapping (Al and Cu signals). c) The line scan across the NW is shown in (c). d) Nanolaminate samples, consisting of alternating ALD layers of Al$_2$O$_3$ and ZnO on Cu NWs. Example STEM image and corresponding EDX mapping (Al, Cu, and Zn signals). e) The line scan across the NW is shown in (e).
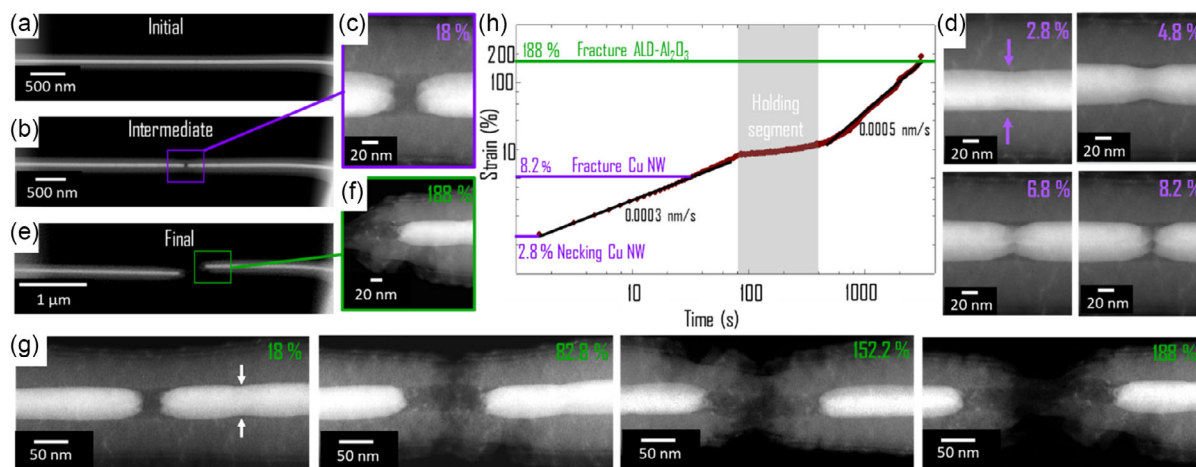
Figure 2. In situ mechanical testing of core–shell samples in TEM. Cu NWs coated with Al$_2$O$_3$. a) Initial conditions before straining. b) Intermediate state. c) Close-up of the failure point. The shell is still intact, the core is already fractured. d) Image sequence from the in situ testing. Plastic deformation of the NW starts at 2.8% strain. e) Final state after testing. f) Close-up of the fractured sample. g) Image sequence from the in situ testing. Failure of the ALD shell after applying 188% strain. The white arrow marks the location of the second necking spot. h) Applied strain during tensile testing. First segment with a strain rate of 0.0003 nm s^{-1} and second segment with 0.0005 nm s^{-1}. An intermediate holding segment was used to readjust the field of view and to take images. See also the supporting in situ video and Figure S1, Supporting Information.
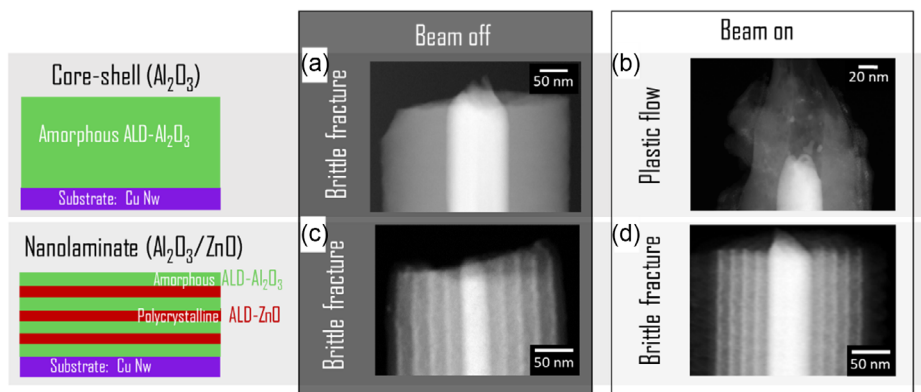
Figure 3. Comparison of core–shell and nanolaminate samples under beam-off (representative STEM image of ex situ tested samples) and beam-on conditions (STEM image of in situ tested samples). a) Brittle fracture of the Al$_2$O$_3$ shell. b) Plastic flow of the Al$_2$O$_3$ shell. c) Brittle fracture of the nanolaminate (beam-off). d) Brittle fracture of the nanolaminate (beam-on).

was not exposed to the electron beam during mechanical loading (Figure 3c). Interestingly, the nanolaminate did not show a plastic behavior under beam-on condition and showed the same brittle behavior which we have observed without electron beam illumination. During the in situ tensile experiment, we see an abrupt brittle cracking, which leads to the complete failure of the sample. The crack propagated straight through the coating, and no significant crack deflection due to the laminated structure or delamination has occurred. In contrast, the NW core deforms plastically. Figure 3d shows exemplarily the difference in the deformation behavior of the metal NW and the nanolaminated coating. The failure of the NW occurs by necking up to a complete narrowing and ending up in ductile fracture. After the failure of the metallic core, the cracking process continues through the coating, initiating complete failure of the nanolaminate.

Due to the ALD process parameters, the Al$_2$O$_3$ layer is amorphous, and the ZnO layer is polycrystalline with grain sizes in the range of 2−6 nm. The crack is initialized during uniaxial straining on the surface of the top Al$_2$O$_3$ layer and propagates through the amorphous material. Reaching the ZnO layer, the crack propagates along the grain boundaries. A long-range crack deflection within the layer has not been observed and the crack passes almost undeflected through the layer. After the brittle fracture of the coating, the crack reaches the metallic core, which deforms plastically via necking. The nanolaminate sample completely fails after straining to only 6%. The coating preserves the metallic core under mechanical load until the crack passes the coating. We do not observe complete delamination at the metal–ALD interface, which indicates a good adhesion of the first Al$_2$O$_3$ layer.

**ADVANCED
SCIENCE NEWS**

www.advancedsciencenews.com

**ADVANCED
ENGINEERING
MATERIALS**

www.aem-journal.com

3.2. EELS Measurements

To characterize the ALD layer and the effect of electron beam irradiation in more detail, we use scanning transmission electron microscopy (STEM)-EELS and characteristic edge fine structure analysis. The shape of the Al L_{2-3} edge depends on the Al coordination and can be used as a fingerprint to distinguish between the crystalline and amorphous phases.[33] **Figure 4**a compares tabulated data[34] for α-Al$_2$O$_3$ (pink line) and γ-Al$_2$O$_3$ (green line) with our acquired data for the ALD-Al$_2$O$_3$ shell. Both crystalline phases show a pronounced maximum at 84 Ev, indicating a medium-range crystalline structure,[35] which is not formed to that extent in the ALD-Al$_2$O$_3$. The α-Al$_2$O$_3$ shows a pronounced peak at 79 eV followed by a less intense peak at 80 eV, which identifies the octahedrally coordinated Al atoms.[36] In contrast to the α-phase, γ-Al$_2$O$_3$ has two configurations, tetrahedrally and octahedrally coordinated Al atoms, resulting in two peaks at 78 and 79.5 eV.[37,38] The ALD- Al$_2$O$_3$ shows a broad maximum centered around 77 eV followed by an intensity peak at 80 eV. Consequently, the spectrum contains signatures of tetrahedrally and octahedrally coordinated Al atoms; however, the altered shape and shift of the onset indicate the presence of distorted bonds.[39] Indeed, the ALD-Al$_2$O$_3$ is amorphous, and during the TEM experiment, no crystallization has been induced. Figure 4b shows the oxygen K-edge of the ALD-Al$_2$O$_3$. The EELS scans have been acquired with different dose rates, to see any effects induced by electron beam irradiation. The oxygen near-edge structure is sensitive to changes within the local bonding environment of Al atoms and gives us insights into the electron-beam-induced mechanism within the amorphous network. All spectra show a broad maximum centered around 540 eV. We increased the electron dose rate from 45 e$^-$/Å^{2}s (Scan 2: blue line) to 68 e$^-$/Å^{2}s to evaluate any beam-induced changes of the oxygen peak. However, even after the scan with the highest dose rate (Scan 4: cyan line), we still do not observe changes within the spectra. To evaluate the effect of illumination similar to the in situ tensile experiment, we perform an additional scan (Scan 5: red line) of the scan area of Scan 4, after illuminating the whole sample for 12 min. However, the additional dose history does not induce any changes in the shape

or in the peak position of the oxygen edge. Together with the Al edge shown in Figure 4a, this suggests that the bond character within the amorphous lattice did not change during the electron beam illumination.

To test the threshold for electron beam damage,[40] we increased the dose significantly, which is displayed in Figure 4c. For the heavily irradiated ALD-Al$_2$O$_3$ (dose rate of the EELS scan: 330 e$^-$/Å^{2}s, total dose: 5.4·10^4 e$^-$/Å^2), the peak position is more pronounced at 544 eV and a second sharp peak at 532 eV appears, which suggests an atomic rearrangement[41] and the presence of a high density of molecular oxygen.[33] This phenomenon is known from electron-beam-induced hole drilling in amorphous Al$_2$O$_3$[42] and can be explained by knock-on damage. The threshold displacement energy of oxygen in Al$_2$O$_3$ is 28 eV and that of aluminum is 25 eV.[43] At an electron energy of 200 keV, the maximum transferrable energy to the respective atoms is 32 eV for oxygen and 19 eV for aluminum.[44] This means that oxygen atoms can be knocked out of their position in the material during irradiation. If the dose rate is high enough, knocked-out oxygen atoms can bond and form molecular oxygen. However, at lower dose rates, no molecular oxygen is detected, hinting at a rebinding to the network of knocked-out atoms. In our in situ experiment, the electron irradiation was significantly lower (2.71 e$^-$/Å^{2}s, total dose: 8.1·10^3 e$^-$/Å^2) than during the EELS acquisition, excluding the formation of molecular oxygen.

4. Discussion

In our experiments, we see an amorphous Al$_2$O$_3$ shell deforming plastically during in situ tensile straining in the TEM, displayed in Figure 2. The Al$_2$O$_3$ remains amorphous, and we did not see any crystallites forming within the shell. However, we did not observe plasticity in samples, which have not been irradiated, see Figure 3. These examined beam-off samples have Al$_2$O$_3$ shells in the range of 5–150 nm thickness, all of which show the same behavior.[45,46] Therefore, we can exclude plasticity arising from a size effect.[45,46] Together with the EELS measurements, this indicates that the plastic behavior of the ALD-Al$_2$O$_3$ is
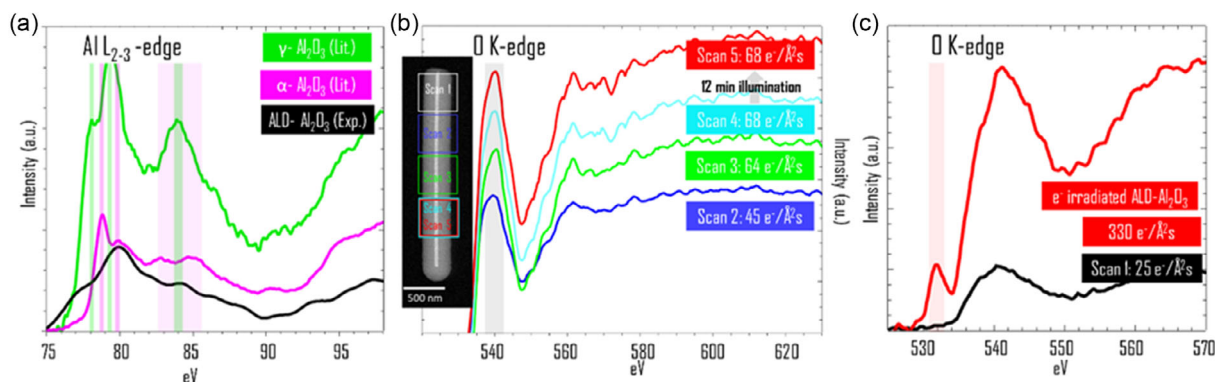
Figure 4. EELS analysis to evaluate any changes induced by the electron beam. a) Aluminum L_{2-3}-edge: Comparison of tabulated spectra[34] for the α- and γ-Al$_2$O$_3$ phase with our samples. Our experimental data (Scan 1: 25 e$^-$/Å^{2}s) are in accordance with amorphous Al$_2$O$_3$. b) Oxygen K-edge with a maximum centered around 540 eV: Comparison of different electron dose rates during the EELS scan. The scan areas are indicated in the STEM image of the core–shell sample. c) Demonstration of electron beam damage induced by a high dose rate of 330 e$^-$/Å^{2}s. A second peak at 532 eV appears.

induced by atomic rearrangement within the lattice provoked by the electron beam. In the following, we will discuss important considerations, which lead us to the conclusion of the bond switch mechanism.

Amorphous Al_2O_3 is approximately 30% less dense compared to their crystalline phases, which already indicates that the amorphous structure is more defective.[47] Nevertheless, for amorphous Al_2O_3, short-range ordering of the oxygen ligands around the central Al atoms within a distorted matrix is reported,[44,48] which is in agreement to the EELS spectra of the Al L_{2-3}-edge showing signatures of tetrahedrally and octahedrally coordinated Al atoms. **Figure 5**a shows schematically an amorphous $ALD-Al_2O_3$ film, with the local ordering of tetrahedrally and octahedrally coordinated Al atoms. The electron beam has several effects on the material, namely ionization, knock-on, and local heating. Local heating can generally be neglected for the parameters used in this study.[49] Ionization, on the other hand, can lead to bond cleavage (Al–O bond energy: 5.2 eV[50]) and therefore dangling bonds within the material.[44] In particular, thermodynamically less stable bonds (e.g. 3- and 5-coordinated Al atoms) are broken, and a spontaneous rearrangement with other bonding partners can occur. Finally, knock-on damage can lead to the formation of oxygen vacancies and interstitials. Atoms adjacent to these defects may form new bonds, leading to a reconfiguration of the local network. Figure 5b shows schematically the changing ALD structure under electron beam irradiation. The combination of bond breakage and connecting to new bonding partners enables the amorphous structure to align in the loading direction and compensate for the applied strain.

Our EELS measurements have been performed with different electron dose rates, and no electron beam-induced damage has been observed for low and medium dose rates. Electron beam damage can be detected by morphological changes of the ALD film, e.g., hole drilling,[41] and by the EELS spectra that show a distinct maximum at 532 eV, indicating the formation of molecular oxygen.[33] With our measurements, we tested the threshold of the irradiation dose for beam damage in our system, displayed in Figure 4c. For the observed plastic flow, we are well-below this critical damage value. Therefore, we conclude that the electron beam activates bond switching within the amorphous network to compensate for the applied strain and induce the high plasticity.

Comparable behavior to what we have shown in our in situ TEM experiments has been reported previously. For example, Frankberg et al.[51] reported a highly ductile behavior for amorphous Al_2O_3 produced by pulsed laser deposition. They performed in situ TEM tensile tests of thin film samples using push-to-pull devices and used atomistic simulations to determine the effect of the strain rate. After carefully considering potential issues affecting the material response, they ruled out electron-beam-induced effects. Nevertheless, their explanation for the high ductility is based on bond switch activities within the dense and flaw-free amorphous network.[51] In contrast, in our study, we clearly see the impact of the electron beam, which induces a transition from brittle to ductile behavior. The reason for the discrepancy might be the nature of the Al_2O_3, as Frankberg et al. used a "flaw-free" glass structure. It is known that layers deposited by ALD contain traces of hydrogen.[52,53] We estimate that at our deposition temperature of 120 °C, we have up to 6%–8% hydrogen in the film and <1% of carbon.[52,54] While the overall nature of the film is that of aluminum oxide, the residual hydrogen may still affect the mechanical properties. A higher hydrogen content is reported to lead to a slightly lower Young's modulus and hardness.[54] However, the deformation mode does not change with the hydrogen content. During electron beam irradiation, hydrogen is quickly lost. This effect leads to a densification of the Al_2O_3 shell, which we observe in our samples (see Figure S2, Supporting Information). After this densification, no further structural changes are observed. We therefore believe that hydrogen incorporated in the layers does not significantly change the response of the material during in situ testing.

The thin film preparation reported by Frankberg et al. via focused ion beam (FIB) for tensile testing indicates a consistent electron beam illumination during sample alignment by scanning electron microscopy. Such details of the sample preparation have a significant impact on the mechanical behavior of glassy structures.[46] The advantage of our study is the use of dedicated small-scale model systems, making the need for extensive sample preparation unnecessary.
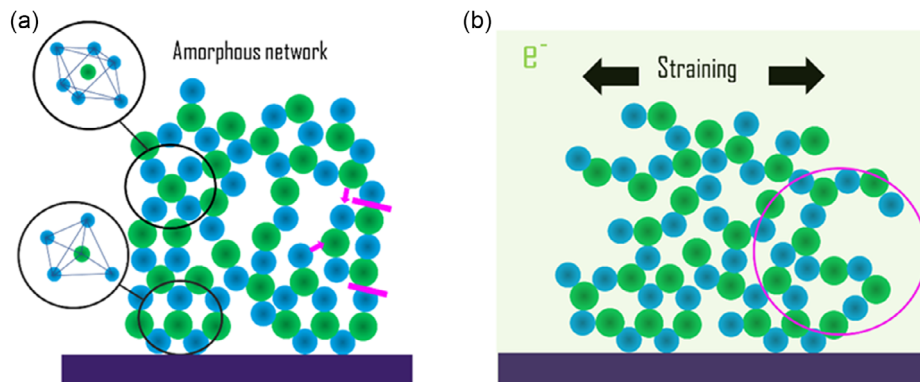
Figure 5. Schematic illustration of the ALD layer and the effect of the electron beam on the amorphous network structure. a) The $ALD-Al_2O_3$ has an amorphous matrix with 4- and 6-coordinated Al atoms. The pink symbols indicate the changing bonds caused by electron beam illumination. b) Bond switch mechanism induced by electron beam irradiation during tensile testing.

Regarding the behavior of the nanolaminates, any electron beam-induced plasticity is not enough to compensate for the inherent brittleness of the nanolaminated structures. The intermediate films of ZnO interrupt the amorphous Al_2O_3, leading to a nanolaminated shell. The fracture behavior of the nanolaminates is dominated by cracking along grain boundaries within the ZnO layer. Indeed, crystalline ZnO does not show electron-beam-induced plasticity, which can be explained by the rigid lattice structure and the inability of bond switching that finally results in brittle fracturing.

5. Conclusion

Tailoring the properties of metal oxide films is one important step for designing coatings for MEMS. By using unique small-scale model systems, we characterized the electron-beam-induced highly plastic behavior of ALD encapsulations. As a substrate, we use Cu NWs, which have been subsequently coated via ALD. Using such nanoscale samples enables us to avoid extensive preparation routines for TEM investigations, which are known to alter the mechanical properties of glass structures. We compare core–shell structures with an amorphous Al_2O_3 shell with nanolaminates consisting of alternating layers of Al_2O_3 and ZnO. Without electron beam illumination, both coatings show brittle fracture. The in situ experiments show that the electron beam has a direct impact on the structure–property relationship of amorphous metal oxides inducing a brittle to ductile transition, which can be explained by a bond switch mechanism. The absence of the highly plastic behavior in the nanolaminate can be explained by the crystalline ZnO, which dominates the failure mechanism. The findings underscore the immense effect of electron beam illumination on the mechanical behavior of amorphous ALD films.

6. Microscopes and Equipment

The TEM study was performed at a Thermo Scientific Titan Themis 200 G3 Empa Thun at 200 kV. The instrument is equipped with a high-performance super-X energy-dispersive X-ray spectroscopy (EDX) system, which was used to map the elemental distribution in our samples. The EELS was performed at the TEAM I at the National Center for Electron Microscopy (NCEM) Berkeley. The in situ mechanical tests were performed with a Gatan single tilt straining holder Model 654. The holder can elongate at a maximum rate of $2.0\,\mu m\,s^{-1}$ with a nominal drift rate of $1.5\,nm\,mm^{-1}$. The holder is purely displacement controlled and does not measure force. The strain has been evaluated by image analysis using a Python script based on template matching[55,56] (further details in Figure S1, Supporting Information). The tensile stripes are made of a 0.5 mm thin copper foil, where we milled a hole with the FIB Tescan Lyra3 (further details in Figure S3, Supporting Information). The sample transfer has been done by using a nanomanipulation system and a gas injection system (carbon precursor). The carbon contamination on the wires is kept to a minimum by limiting the e-beam exposure during preparation. In addition, after precursor usage, we waited until the base pressure was reached again before continuing operation.

To analyze the effect of the electron beam (off-beam condition), samples have been mechanically transferred to TEM grids (Cu grids with carbon support film). During mechanical transfer, some NWs were exposed to mechanical load. The Cu NWs have been produced with a Mantis Deposition Ltd., QPrep500, UK. The ALD depositions were done at an SC-2 Series from Swiss Cluster AG, Switzerland.

Conflict of Interest

The authors declare no conflict of interest.

Data Availability Statement

The data that support the findings of this study are available from the corresponding author upon reasonable request.

[1] M. Stueber, H. Holleck, H. Leiste, K. Seemann, S. Ulrich, C. Ziebert, *J. Alloys Compd.* **2009**, *483*, 321.

[2] V. Kalancha, A. These, L. Vogl, I. Levchuk, X. Zhou, M. Barr, M. Bruns, J. Bachmann, S. Virtanen, E. Spiecker, A. Osvet, C. J. Brabec, K. Forberich, *Adv. Electron. Mater.* **2022**, *8*, 2100787.

[3] P. H. Mayrhofer, C. Mitterer, L. Hultman, H. Clemens, *Prog. Mater. Sci.* **2006**, *51*, 1032.

[4] J. Geng, L. Shi, J. Ni, Q. Jia, W. Yan, M. Qiu, *PhotoniX* **2022**, *3*, 14.

[5] Y. Lin, F. Duan, J. Pan, C. Zhang, Q. Chen, J. Lu, L. Liu, *Mater. Sci. Eng. A* **2022**, *844*, 143170.

[6] P. Carvalho, P. Sampaio, S. Azevedo, C. Vaz, J. Espinós, V. Teixeira, J. Carneiro, *Appl. Surf. Sci.* **2014**, *307*, 548.

[7] N. D. Hoivik, J. W. Elam, R. J. Linderman, V. M. Bright, S. M. George, Y. C. Lee, *Sens. Actuators A* **2003**, *103*, 100.

[8] F. Buja, G. Fiorentino, J. Kokorian, W. M. van Spengen, *Nanotechnology* **2015**, *26*, 255701.

[9] R. L. Puurunen, J. Saarilahti, H. Kattelus, *ECS Trans.* **2007**, *11*, 3.

[10] C. R. Stoldt, V. M. Bright, *J. Phys. D: Appl. Phys.* **2006**, *39*, R163.

[11] V. Miikkulainen, M. Leskelä, M. Ritala, R. L. Puurunen, *J. Appl. Phys.* **2013**, *113*, 021301.

[12] R. L. Puurunen, *J. Appl. Phys.* **2005**, *97*, 121301.

[13] L. Zhang, H. C. Jiang, C. Liu, J. W. Dong, P. Chow, *J. Phys. D: Appl. Phys.* **2007**, *40*, 3707.

[14] M. D. Groner, J. W. Elam, F. H. Fabreguette, S. M. George, *Thin Solid Films* **2002**, *413*, 186.

[15] M. Berdova, O. M. E. Ylivaara, V. Rontu, P. T. Törmä, R. L. Puurunen, S. Franssila, *J. Vac. Sci. Technol. A* **2015**, *33*, 01A106.

[16] S.-H. Jen, J. A. Bertrand, S. M. George, *J. Appl. Phys.* **2011**, *109*, 084305.

[17] V. Chawla, M. Ruoho, M. Weber, A. A. Chaaya, A. A. Taylor, C. Charmette, P. Miele, M. Bechelany, J. Michler, I. Utke, *Nanomaterials* **2019**, *9*, 88.

[18] J. Koo, S. Lee, J. Kim, D. H. Kim, B.-H. Choi, T.-S. Kim, J. H. Shim, *Scr. Mater.* **2020**, *187*, 256.

[19] S. J. Bull, *J. Vac. Sci. Technol. A* **2012**, *30*, 01A160.

[20] N. F. Mott, *Lond. Edinb. Dublin Philos. Mag. J. Sci.* **1952**, *43*, 1151.

[21] E. Hall, *Proc. Phys. Soc. B* **1951**, *64*, 747.

[22] R. A. B. Devine, J. Arndt, *Phys. Rev. B* **1989**, *39*, 5132.

[23] N. F. Borrelli, C. Smith, D. C. Allan, T. P. Seward, *J. Opt. Soc. Am. B* **1997**, *14*, 1606.

[24] F. Piao, W. G. Oldham, E. E. Haller, *J. Non-Cryst. Solids* **2000**, *276*, 61.

[25] M. Mačković, F. Niekiel, L. Wondraczek, E. Spiecker, *Acta Mater.* **2014**, *79*, 363.

[26] K. Zheng, C. Wang, Y.-Q. Cheng, Y. Yue, X. Han, Z. Zhang, Z. Shan, S. X. Mao, M. Ye, Y. Yin, E. Ma, *Nat. Commun.* **2010**, *1*, 24.

[27] L. M. Vogl, P. Schweizer, L. Pethö, A. Sharma, J. Michler, I. Utke, *Nanoscale* **2023**, *15*, 9477.

[28] G. Richter, K. Hillerich, D. S. Gianola, R. Mönig, O. Kraft, C. A. Volkert, *Nano Lett.* **2009**, *9*, 3048.

[29] L. M. Vogl, P. Schweizer, P. Denninger, G. Richter, E. Spiecker, *ACS Nano* **2022**, *16*, 18110.

[30] J. Dendooven, C. Detavernier, in *Atomic Layer Deposition in Energy Conversion Applications*, Wiley-VCH Verlag, Weinheim, Germany **2017**, p. 1.

[31] T. Tynell, M. Karppinen, *Semicond. Sci. Technol.* **2014**, *29*, 043001.

[32] J. W. Elam, S. M. George, *Chem. Mater.* **2003**, *15*, 1020.

[33] D. Bouchet, C. Colliex, *Ultramicroscopy* **2003**, *96*, 139.

[34] P. Ewels, T. Sikora, V. Serin, C. P. Ewels, L. Lajaunie, *Microsc. Microanal.* **2016**, *22*, 717.

[35] A. Balzarotti, A. Bianconi, E. Burattini, M. Grandolfo, R. Habel, M. Piacentini, *Phys. Status Solidi B* **1974**, *63*, 77.

[36] E. Schilirò, P. Fiorenza, C. Bongiorno, C. Spinella, S. Di Franco, G. Greco, R. Lo Nigro, F. Roccaforte, *AIP Adv.* **2020**, *10*, 125017.

[37] K. Kimoto, Y. Matsui, T. Nabatame, T. Yasuda, T. Mizoguchi, I. Tanaka, A. Toriumi, *Appl. Phys. Lett.* **2003**, *83*, 4306.

[38] S. Fritz, A. Seiler, L. Radtke, R. Schneider, M. Weides, G. Weiß, D. Gerthsen, *Sci. Rep.* **2018**, *8*, 7956.

[39] L. Zeng, D. T. Tran, C.-W. Tai, G. Svensson, E. Olsson, *Sci. Rep.* **2016**, *6*, 29679.

[40] A. M. Jasim, X. He, Y. Xing, T. A. White, M. J. Young, *ACS Omega* **2021**, *6*, 8986.

[41] S. D. Berger, I. G. Salisbury, R. H. Milne, D. Imeson, C. J. Humphreys, *Philos. Mag. B* **1987**, *55*, 341.

[42] C. J. Humphreys, T. J. Bullough, R. W. Devenish, D. M. Maher, P. S. Turner, *Scanning Microsc.* **1990**, *1990*, 13.

[43] D. Loiacono, M. Vanazzi, B. Paladino, W.-Y. Chen, M. Cabrioli, M. Li, M. G. Beghi, F. Di Fonzo, *J. Nucl. Mater.* **2024**, *588*, 154805.

[44] R. Nakamura, M. Ishimaru, H. Yasuda, H. Nakajima, *J. Appl. Phys.* **2013**, *113*, 064312.

[45] Y. Yang, A. Kushima, W. Han, H. Xin, J. Li, *Nano Lett.* **2018**, *18*, 2492.

[46] J. Luo, J. Wang, E. Bitzek, J. Y. Huang, H. Zheng, L. Tong, Q. Yang, J. Li, S. X. Mao, *Nano Lett.* **2016**, *16*, 105.

[47] R. Nakamura, T. Toda, S. Tsukui, M. Tane, M. Ishimaru, T. Suzuki, H. Nakajima, *J. Appl. Phys.* **2014**, *116*, 033504.

[48] P. C. Snijders, L. P. H. Jeurgens, W. G. Sloof, *Surf. Sci.* **2005**, *589*, 98.

[49] R. F. Egerton, P. Li, M. Malac, *Micron* **2004**, *35*, 399.

[50] Y.-R. Luo, *Comprehensive Handbook of Chemical Bond Energies*, CRC Press, Boca Raton, FL **2007**.

[51] E. J. Frankberg, J. Kalikka, F. García Ferré, L. Joly-Pottuz, T. Salminen, J. Hintikka, M. Hokka, S. Koneti, T. Douillard, B. Le Saint, P. Kreiml, M. J. Cordill, T. Epicier, D. Stauffer, M. Vanazzi, L. Roiban, J. Akola, F. Di Fonzo, E. Levänen, K. Masenelli-Varlot, *Science* **2019**, *366*, 864.

[52] C. Guerra-Nuñez, M. Döbeli, J. Michler, I. Utke, *Chem. Mater.* **2017**, *29*, 8690.

[53] M. Groner, F. Fabreguette, J. Elam, S. M. George, *Chem. Mater.* **2004**, *16*, 639.

[54] O. M. E. Ylivaara, X. Liu, L. Kilpi, J. Lyytinen, D. Schneider, M. Laitinen, J. Julin, S. Ali, S. Sintonen, M. Berdova, E. Haimi, T. Sajavaara, H. Ronkainen, H. Lipsanen, J. Koskinen, S.-P. Hannula, R. L. Puurunen, *Thin Solid Films* **2014**, *552*, 124.

[55] L. M. Vogl, P. Schweizer, M. Wu, E. Spiecker, *Nanoscale* **2019**, *11*, 11687.

[56] L. M. Vogl, P. Schweizer, G. Richter, E. Spiecker, *MRS Adv.* **2021**, *6*, 665.